nature geoscience

Article

https://doi.org/10.1038/s41561-023-01144-z

Surface warming and wetting due to methane's long-wave radiative effects muted by short-wave absorption

In the format provided by the authors and unedited

Contents of this file

Supplementary Note 1: CESM2 CH_4 warming versus IPCC

Supplementary Note 2: Apparent hydrological sensitivity

Supplementary Note 3: 5xCH_4 and 2xCH_4 ERF

Supplementary Note 4: Surface and atmospheric radiation contributions to ERF

Supplementary Note 5: Surface and atmospheric rapid adjustments for 10xCH_4

Supplementary Note 6: Rapid Adjustments using the CloudSat/CALIPSO kernel

Supplementary Note 7: Cloud feedback under CH_{4SW}

Supplementary Note 8: 3xCH_4 PDRMIP results

Supplementary Note 9: Contribution of land surface warming/cooling to ERF

Supplementary References

Figures S1 to S8

Supplementary Note 1: CESM2 CH_4 warming versus IPCC

As mentioned in the main text, we estimate 0.17 K of global warming in response to present-day CH_{4LW+SW} (relative to preindustrial) based on CESM2 simulations (Figure 1). This is less than that from the newest IPCC AR6 report at 0.28 K, with a 5-95% range of 0.19 to 0.39 K (1). This underestimation is in part due to the fact the CH_{4LW+SW} ERF in CESM2 (for a 0.75 to 1.8 ppm perturbation, i.e., 2.4xCH_4) is also below the corresponding AR6 estimate of 0.55 (0.44 to 0.66) W m^{-2}. For CESM2 simulations, the 2xCH_{4LW+SW} experiment has an ERF of 0.35 W m^{-2} (Extended Data Figure 3g) and 5xCH_{4LW+SW} has an ERF of 0.98 W m^{-2} (Extended Data Figure 3d). A square root dependence of ERF on methane concentrations gives ∼0.4-0.45 W m^{-2}. This plus the fact that the CESM2 coupled simulations likely aren't in true equilibrium after 90 years leads to temperature estimates that fall below the AR6 range.

We also note that our regression fit in Figure 1a,b includes the zero ΔCH_4 and zero change in near-surface air temperature (or zero change in precipitation) data point. However, we do not force the regression intercept to be zero. This is based on the fact the 2x, 5x and 10xCH_4 points aren't exactly on the regression line, so we assume the 1xCH_4 doesn't need to be either. Nonetheless, constraining the regression intercept to be zero and repeating the analysis yields less CH_{4LW+SW} warming (0.13 versus 0.17 K), similar CH_{4LW} warming (0.20 K for both), and larger CH_{4SW} cooling (−0.07 versus −0.04 K). For precipitation, forcing the regression intercept to zero yields a smaller increase in CH_{4LW+SW} precipitation (0.13 versus 0.16%), a larger CH_{4LW} precipitation increase (0.35 versus 0.31%) and a larger CH_{4SW} precipitation decrease (−0.22 versus −0.15%). Similarly, the apparent hydrological sensitivity increases under CH_{4LW+SW} and CH_{4LW} (1.02 versus 0.97 % K^{-1} and 1.76 versus

1.51 % K^{-1}) and decreases under CH_{4SW} (3.2 versus 4.3 % K^{-1}).

Supplementary Note 2: Apparent hydrological sensitivity

CH_{4SW} yields relatively large values (compared to CH_{4LW}) for the apparent hydrological sensitivity (AHS; defined as the change in precipitation divided by the change in surface temperature) (2). Under 10xCH_4, the AHS is 1.7% K^{-1} for CH_{4LW}, versus 3.3% K^{-1} for CH_{4SW}. Because precipitation is reduced under CH_4 SW absorption (particularly per unit change in global temperature), the corresponding CH_{4LW+SW} AHS is muted at 1% K^{-1}. Similar values are obtained for 5xCH_4, with an AHS of 1.8% K^{-1} for CH_{4LW}; 3.0% K^{-1} for CH_{4SW}; and 1.1% K^{-1} for CH_{4LW+SW}.

Prior PDRMIP analyses (3; 4) found a larger multi-model AHS in response to 3xCH_4 (for most PDRMIP models this is relative to present-day CH_4) of 1.7±0.4% K^{-1}. However, of the 9 PDRMIP models analyzed, only 4 included an explicit treatment of CH_4 SW absorption (5). Our decomposition (i.e., CH_4 SW radiative effects mute the total AHS) helps to explain the larger apparent hydrological sensitivity to methane in PDRMIP models (see Supplementary Note 6 for additional details).

Our results are also consistent with prior studies that show a strong link between SW absorption (i.e., from absorbing aerosols like black carbon) and precipitation, including relatively large (absolute) values for the apparent hydrological sensitivity (3; 4; 6). Under LW-forcers (e.g., CO_2), the fast and slow precipitation responses counteract one another. Atmospheric absorption yields a decrease in precipitation; surface warming yields an increase (which dominates the overall response). In contrast, methane SW absorption yields a decrease in precipitation due to both atmospheric absorption and surface cooling.

Supplementary Note 3: 5xCH_4 and 2xCH_4 ERF

5xCH_{4LW+SW} yields an ERF of 0.98 W m^{-2}, including 1.19 W m^{-2} for 5xCH_{4LW} and −0.22 W m^{-2} for 5xCH_{4SW} (Extended Data Figure 3). Thus, 5xCH_{4SW} reduces the 5xCH_{4LW} ERF by 18%. For 2xCH_{4LW+SW}, the ERF is 0.35 W m^{-2}, including 0.45 W m^{-2} for 2xCH_{4LW} and −0.09 W m^{-2} for 2xCH_{4SW}. Thus, 2xCH_{4SW} reduces the 2xCH_{4LW} ERF by 20%. All values are significant at the 99% confidence level, except for the 2xCH_{4SW} ERF, which is not significant at the 90% confidence level.

Radiative flux components are also further decomposed into TOA LW and SW radiation (Extended Data Figure 3). For each methane perturbation, the rapid adjustment due to CH_{4SW} is negative for both TOA LW and TOA SW radiation, with somewhat larger negative values for SW fluxes.

Supplementary Note 4: Surface and atmospheric radiation contributions to ERF

The bulk of the negative 10xCH_{4SW} ERF (Fig. 2a) occurs at the surface, due to a reduction in surface net radiative flux (RNET; Supplementary Figure 1a). This is due to a relatively large negative surface IRF at −0.45 W m^{-2} (Supplementary Figure 1a), as the atmospheric IRF is 0.72 W m^{-2} (Supplementary Figure 1d), consistent with a vertical redistribution of SW flux from the surface to the atmosphere (as with other SW absorbers, like black carbon (7; 8; 9; 10; 11)). The rapid adjustment at the surface, which is also negative at −0.30 W m^{-2}, reinforces the negative surface IRF. This vertical redistribution of SW radiation contributes to the strong surface cooling under CH_4 SW absorption (combined with the elevated atmospheric heating).

Supplementary Note 5: Surface and atmospheric rapid adjustments for 10xCH_4

As mentioned in the main text, a negative net radiative flux at the surface (RNET) occurs under 10xCH_{4SW} (Supplementary Figure 1a), in part due to the vertical redistribution of SW flux from the surface to the atmosphere. The decomposition of surface (and atmospheric) rapid adjustments for 10xCH_{4SW} (Supplementary Figure 2a-c) shows that this relatively large (negative) surface net radiation flux is once again largely due to a negative cloud adjustment at the surface, particularly associated with SW radiation (Supplementary Figure 2c). For example, the total surface cloud adjustment under 10xCH_{4SW} is -0.31 W m^{-2} (Supplementary Figure 2a), with a corresponding surface SW cloud adjustment of -0.51 W m^{-2} (Supplementary Figure 2c).

Supplementary Note 6: Rapid Adjustments using the CloudSat/CALIPSO kernel

Recent analyses (5; 12) have shown similar results across different kernels, including the GFDL kernel used here, as well as the CESM (13), HadGEM3 (14) and CloudSat/CALIPSO (15) radiative kernels. Nonetheless, we repeat our rapid adjustment calculations with the CloudSat/CALIPSO (15) radiative kernel. Extended Data Figure 5 shows very similar TOA rapid adjustments based on the CloudSat/CALIPSO radiative kernel, as compared to the GFDL kernel. Based on 10xCH_{4LW+SW} (Extended Data Figure 5a), the total rapid adjustment is -0.40 and -0.36 W m^{-2} based on the GFDL and CloudSat/CALIPSO radiative kernel, respectively. The corresponding total rapid adjustments for 10xCH_{4SW} are -0.77 and -0.71 W m^{-2}. And more importantly, the cloud rapid adjustments are also similar. For

$10xCH_{4SW}$, the cloud rapid adjustment is -0.58 and -0.57 W m^{-2} based on the GFDL and CloudSat/CALIPSO radiative kernel, respectively. The two kernels also yield similar rapid adjustments under 5x and $2xCH_4$ (Extended Data Figure 5b,c).

Supplementary Note 7: Cloud feedback under CH_{4SW}

The $10xCH_{4SW}$ cloud feedback is dominated by increases in low-level (and mid-level) clouds, with weaker decreases in high-level clouds (Supplementary Figure 6d). For example, vertically-integrated low clouds (surface to 700a hPa) significantly increase by 0.42% and 0.36% due to slow and fast responses, respectively. The corresponding change in high clouds (400 hPa to model top) is -0.09% (not significant at the 90% confidence level) and -0.57%. The importance of low clouds (which primarily impact SW radiation) to the slow feedback response is also suggested by the TOA SW versus LW cloud feedback−the TOA LW cloud feedback is only 0.03 W m^{-2}, whereas the TOA SW cloud feedback is -0.40 W m^{-2} (not shown). Similar results exist for $5xCH_{4SW}$ (Supplementary Figure 7d), but weaker results exist for $2xCH_{4SW}$ (Supplementary Figure 8d). For example, the low-, mid- and high-level $2xCH_{4SW}$ cloud feedbacks are not significant. Thus, for larger CH_4 perturbations (e.g., 10x and $5xCH_{4SW}$), surface temperature induced cloud feedbacks act to reinforce the cooling due to cloud rapid adjustments. We briefly note that most of the surface temperature-induced increase in low cloud cover occurs over marine stratocumulus regions (e.g., off the west coasts of North and South America; not shown), consistent with a low-level cloud positive (as traditionally defined, i.e., normalized by surface temperature) feedback (16; 17).

Supplementary Note 8: $3xCH_4$ PDRMIP results

Expanding upon (5), we find that PDRMIP 3xCH_4 simulations yield very similar results to those presented here (based on our CESM2/CAM6 5x and 10xCH_4 simulations). Note that most (but not all) PDRMIP models use year ∼2000 as the base year (i.e., the PDRMIP 3xCH_4 perturbation is similar to our 5xCH_4 perturbation). We separate PDRMIP models into two subsets−4 models (CanESM2, MIROC-SPRINTARS, MPI-ESM and NCAR-CESM1-CAM5) that include an explicit representation of CH_4 SW radiative effects versus 6 models (GISS-E2-1-R, HadGEM2-ES, HadGEM3, IPSL-CM5A, NCAR-CESM1-CAM4, NorESM1) that only include CH_4 LW radiative effects (e.g., see Supplementary Table 1 of (5)).

Methane SW radiative effects are inferred from the difference of these two model subsets (i.e., CH_4 SW+LW radiative effect models minus CH_4 LW radiative effect models). As noted in the main text, such a difference will include other model differences that could complicate the interpretation. However, we find that this indirect assessment yields similar conclusions as to those based on our targeted (and systematic) CESM2/CAM6 simulations. For example, Extended Data Figure 8b shows that 3xCH_4 PDRMIP models that include CH_4 SW radiative effects yield global warming (in the coupled simulations, which includes IRF, adjustments and feedbacks) of 0.48±0.12 K; models that include CH_4 LW radiative effects only yield larger warming of 0.87±0.30 K. Thus, the inferred impact of CH_4 SW radiative effects is −0.39±0.32 K. This represents 45% less warming, which is similar to (but somewhat larger than) what we obtain with CESM2 for 5x and 10xCH_{4SW} at ∼30%.

For precipitation (Extended Data Figure 8c), PDRMIP models yield an inferred decrease of precipitation of −1.24±0.9% due to CH_4 SW radiative effects (in the coupled simulations, i.e., including IRF, adjustments and feedbacks), which represents 65% less wetting (compared

to PDRMIP models with CH_4 LW radiative effects only). Our CESM2 simulations for 5x and 10xCH_{4SW} yield ∼60% less wetting.

The larger impact on precipitation (relative to temperature) also effects the apparent hydrological sensitivity (AHS; Extended Data Figure 8d). PDRMIP models that include CH_4 LW radiative effects yield a larger AHS (2.08±0.49% K^{-1}) relative to models that include both SW and LW CH_4 radiative effects (1.34±0.26% K^{-1}). Thus, PDRMIP models that include methane LW and SW radiative effects yield a 36% decrease in AHS, relative to models that include methane LW radiative effects only. Our CESM2 simulations for 10xCH_{4SW} and 5xCH_{4SW} yield similar AHS decreases at 41% and 39%, respectively.

Calculating the inferred AHS due to CH_4 SW radiative effects as the difference (SW+LW CH_4 models minus LW CH_4 models) of the multi-model mean precipitation response divided by the corresponding difference (SW+LW CH_4 models minus LW CH_4 models) of the multi-model mean near-surface air temperature response yields an apparent hydrological sensitivity of 3.17±0.55% K^{-1}. This inferred estimate for AHS due to CH_4 SW radiative effects is again in good agreement with that directly calculated from CESM2 simulations at 3.3% K^{-1} for 10xCH_{4SW} and 3.0% K^{-1} for 5xCH_{4SW}.

The muted warming and wetting in PDRMIP models that include CH_4 SW radiative effects is consistent with their weaker effective radiative forcing (from fSST simulations) at 1.0±0.26 W m^{-2}, relative to CH_4 LW radiative effect models at 1.24±0.16 W m^{-2} (Extended Data Figure 8a). This represents a 20% decrease in ERF, which is again consistent with our targeted CAM6 fSST simulations, which yield a ∼20% decrease in ERF for 10xCH_{4SW} and 2xCH_{4SW}, and 18% for 5xCH_{4SW}.

Supplementary Note 9: Contribution of land surface warming/cooling to ERF

The climatological-SST method of deriving ERF includes the TOA flux changes resulting from perturbed land surface temperatures as part of the ERF. This is because prescribing land surface temperatures remains difficult to implement in climate models. As with most other studies (5; 18), this has not been performed here.

One can, however, approximate the impact of perturbed land surface temperatures on ERF via the "land-surface-corrected effective radiative forcing (ERF_{ts})" (18). Here, the land surface temperature change adjustment is subtracted from the default (climatological-SST) ERF using the surface temperature radiative kernel. We note that this can be taken farther, e.g., by estimating the "tropospherically corrected effective radiative forcing (ERF_{trop})", which also removes the proportion of tropospheric temperature and water vapor change associated with the land surface temperature change (the surface albedo change is also removed) (18).

Figure 2b (for 10xCH_4) shows the surface temperature adjustment (purple bars) is -0.08 W m^{-2} for CH_{4LW+SW}; -0.09 W m^{-2} for CH_{4LW}; and 0.01 W m^{-2} for CH_{4SW}. Thus, the surface temperature adjustment is relatively small (particularly for 10xCH_{4SW}), being 4.7%, 4.2% and 2.3% of the ERF for 10xCH_{4LW+SW}, 10xCH_{4LW} and 10xCH_{4SW}, respectively. Similarly, the surface temperature adjustments are <5% of the ERF for 5xCH_4 and 2xCH_4 (e.g., Extended Data Figure 4 shows the corresponding surface temperature adjustments).

SUPPLEMENTARY REFERENCES

[1] Forster, P. *et al.* The Earth's Energy Budget, Climate Feedbacks, and Climate Sensitivity. In Climate Change 2021: The Physical Science Basis. Contribution of Working Group I to the Sixth Assessment Report of the Intergovernmental Panel on Climate Change [Masson-Delmotte, V., P. Zhai, A. Pirani, S.L. Connors, C. Péan, S. Berger, N. Caud, Y. Chen, L. Goldfarb, M.I. Gomis, M. Huang, K. Leitzell, E. Lonnoy, J.B.R. Matthews, T.K. Maycock, T. Waterfield, O. Yelekçi, R. Yu, and B. Zhou (eds.)]. Tech. Rep., Cambridge University Press, Cambridge, United Kingdom and New York, NY, USA, pp. 923-1054, doi: :10.1017/9781009157896.009 (2021).

[2] Fläschner, D., Mauritsen, T. & Stevens, B. Understanding the intermodel spread in global-mean hydrological sensitivity. *Journal of Climate* **29**, 801–817, doi: 0.1175/JCLI–D–15–0351.1 (2016).

[3] Samset, B. H. *et al.* Fast and slow precipitation responses to individual climate forcers: A PDRMIP multimodel study. *Geophysical Research Letters* **43**, 2782–2791, 10.1002/2016GL068064 (2016).

[4] Samset, B. H. *et al.* Weak hydrological sensitivity to temperature change over land, independent of climate forcing. *npj Climate and Atmospheric Science* **1**, 20173, doi: 10.1038/s41612–017–0005–5 (2018).

[5] Smith, C. J. *et al.* Understanding rapid adjustments to diverse forcing agents. *Geophysical Research Letters* **45**, 12023–12031, doi: 10.1029/2018GL079826 (2018).

[6] Sand, M., Samset, B. H., Tsigaridis, K., Bauer, S. E. & Myhre, G. Black carbon and precipitation: An energetics perspective. *Journal of Geophysical Research: Atmospheres* **125**, e2019JD032239, doi: 10.1029/2019JD032239 (2020).

[7] Samset, B. H. *et al.* Black carbon vertical profiles strongly affect its radiative forcing uncertainty. *Atmospheric Chemistry and Physics* **13**, 2423–2434, doi: 10.5194/acp–13–2423–2013 (2013).

[8] Samset, B. H. & Myhre, G. Climate response to externally mixed black carbon as a function of altitude. *Journal of Geophysical Research: Atmospheres* **120**, 2913–2927, 10.1002/2014JD022849 (2015).

[9] Allen, R. J. & Landuyt, W. The vertical distribution of black carbon in CMIP5 models: Comparison to observations and the importance of convective transport. *Journal of Geophysical Research: Atmospheres* **119**, 4808–4835, 10.1002/2014JD021595 (2014).

[10] Stjern, C. W. *et al.* Rapid adjustments cause weak surface temperature response to increased black carbon concentrations. *Journal of Geophysical Research: Atmospheres* **122**, 11,462–11,481, doi: 10.1002/2017JD027326 (2017).

[11] Allen, R. J. *et al.* Observationally-constrained aerosol-cloud semi-direct effects. *npj Climate and Atmospheric Science* **2**, doi: 10.1038/s41612–019–0073–9 (2019).

[12] Thornhill, G. D. *et al.* Effective radiative forcing from emissions of reactive gases and

aerosols – a multi-model comparison. *Atmospheric Chemistry and Physics* **21**, 853–874, doi: 10.5194/acp–21–853–2021 (2021).

[13] Pendergrass, A. G., Conley, A. & Vitt, F. M. Surface and top-of-atmosphere radiative feedback kernels for CESM-CAM5. *Earth System Science Data* **10**, 317–324, doi: 10.5194/essd–10–317–2018 (2018).

[14] Smith, C. J., Kramer, R. J. & Sima, A. The HadGEM3-GA7.1 radiative kernel: the importance of a well-resolved stratosphere. *Earth System Science Data* **12**, 2157–2168, doi: 10.5194/essd–12–2157–2020 (2020).

[15] Kramer, R. J., Matus, A. V., Soden, B. J. & L'Ecuyer, T. S. Observation-based radiative kernels from CloudSat/CALIPSO. *Journal of Geophysical Research: Atmospheres* **124**, 5431–5444, doi: 10.1029/2018JD029021 (2019).

[16] Clement, A., Burgman, R. & Norris, J. R. Observational and model evidence for positive low-level cloud feedback. *Science* **325**, 460–464, doi: 10.1126/science.1171255 (2009).

[17] Zelinka, M. D. *et al.* Causes of higher climate sensitivity in CMIP6 models. *Geophysical Research Letters* **47**, e2019GL085782, doi: 10.1029/2019GL085782 (2020).

[18] Smith, C. J. *et al.* Effective radiative forcing and adjustments in CMIP6 models. *Atmospheric Chemistry and Physics* **20**, 9591–9618, doi: 10.5194/acp–20–9591–2020 (2020).

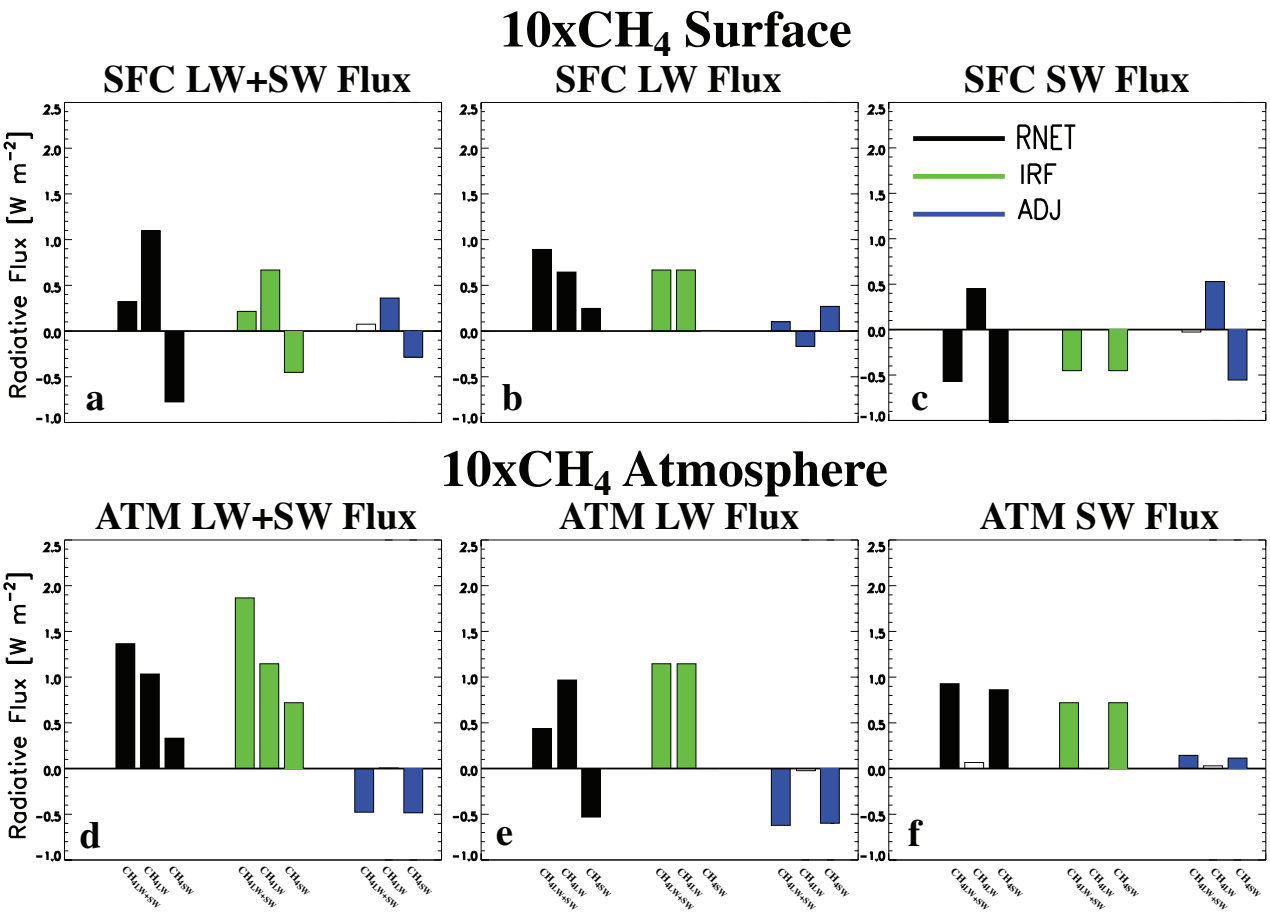

SUPPLEMENTARY FIGURE 1 **Surface and atmosphere radiative flux components in response to 10xCH$_4$.** Global annual mean (a-c) surface and (d-f) atmosphere radiative flux components for 10xCH$_4$. Radiative components include the net radiative flux (RNET; black), instantaneous radiative forcing (IRF; green) and rapid adjustment (ADJ; blue) for (a, d) LW+SW, (b, e) LW and (c, f) SW radiative fluxes. The first bar in each like-colored set of three bars represents the contribution from 10xCH$_{4LW+SW}$; the second bar represents 10xCH$_{4LW}$; and the third bar represents 10xCH$_{4SW}$. Responses not significant, based on a standard t-test at the 90% confidence level, have unfilled bars. These uncertainties are therefore relative to interannual variability. Units are W m^{-2}. Net radiative flux at the surface is estimated as the net surface energy imbalance from the fixed SST experiments. At the atmosphere, it is estimated as the difference between the TOA (i.e., ERF) and surface RNET values. IRF is estimated using an offline radiative transfer model, PORT. The total rapid adjustment is estimated as the sum of individual rapid adjustments from the radiative kernel decomposition. The atmospheric rapid adjustment is estimated as the TOA minus surface difference.

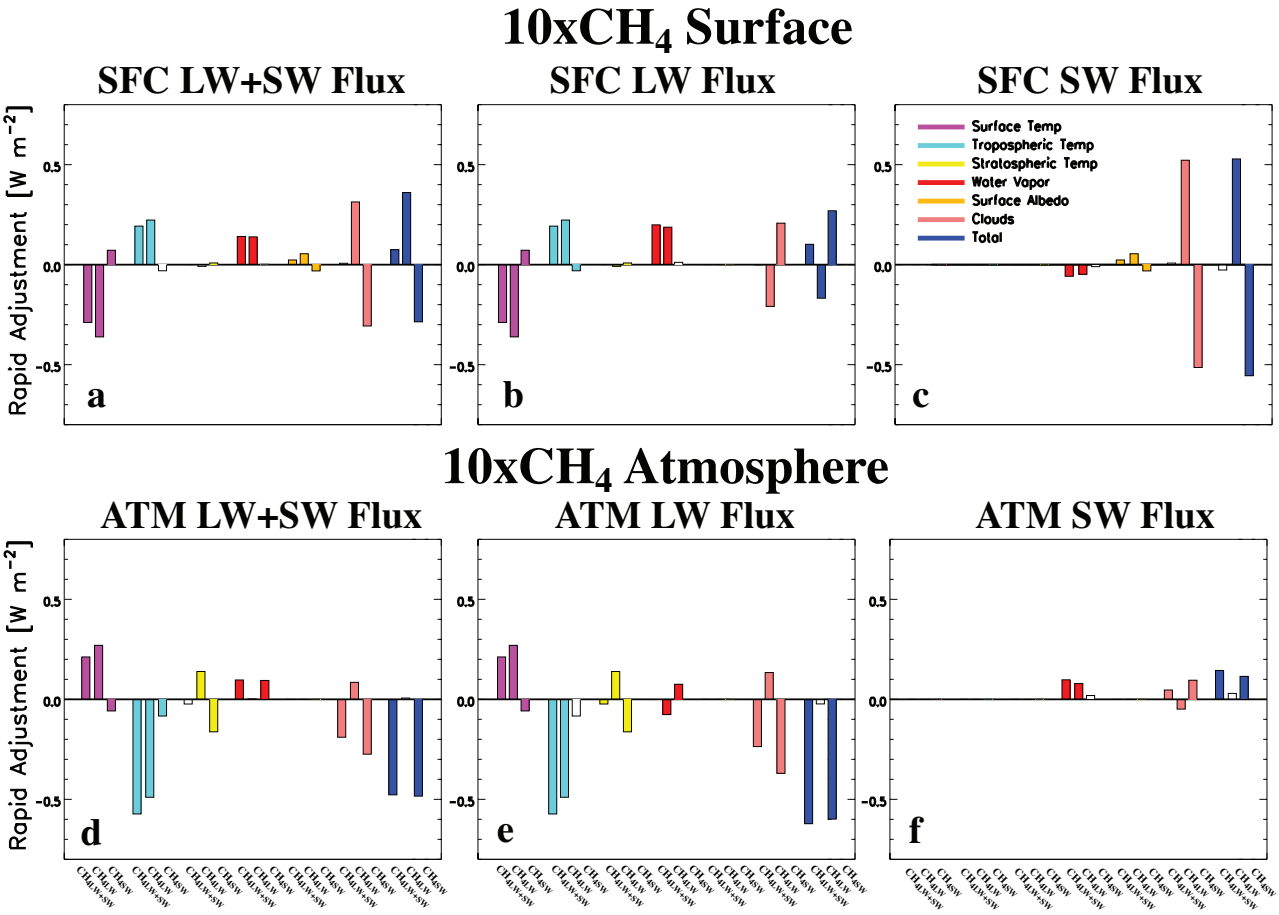

SUPPLEMENTARY FIGURE 2 **Surface and atmosphere rapid adjustment decomposition for 10xCH$_4$.** Global annual mean (a-c) surface and (d-f) atmosphere rapid adjustment decomposition showing the surface temperature (purple), tropospheric temperature (cyan), stratospheric temperature (yellow), water vapor (red), surface albedo (orange), cloud (pink) and total (blue) rapid adjustment for 10xCH$_4$ for (a, d) LW+SW, (b, e) LW and (c, f) SW radiative fluxes. The first bar in each like-colored set of three bars represents the contribution from 10xCH$_{4\mathrm{LW+SW}}$; the second bar represents 10xCH$_{4\mathrm{LW}}$; and the third bar represents 10xCH$_{4\mathrm{SW}}$. Responses not significant, based on a standard t-test at the 90% confidence level, have unfilled bars. These uncertainties are therefore relative to interannual variability. Units are W m^{-2}. The total rapid adjustment is estimated as the sum of individual rapid adjustments from the radiative kernel decomposition. The atmospheric rapid adjustment is estimated as the TOA minus surface difference.

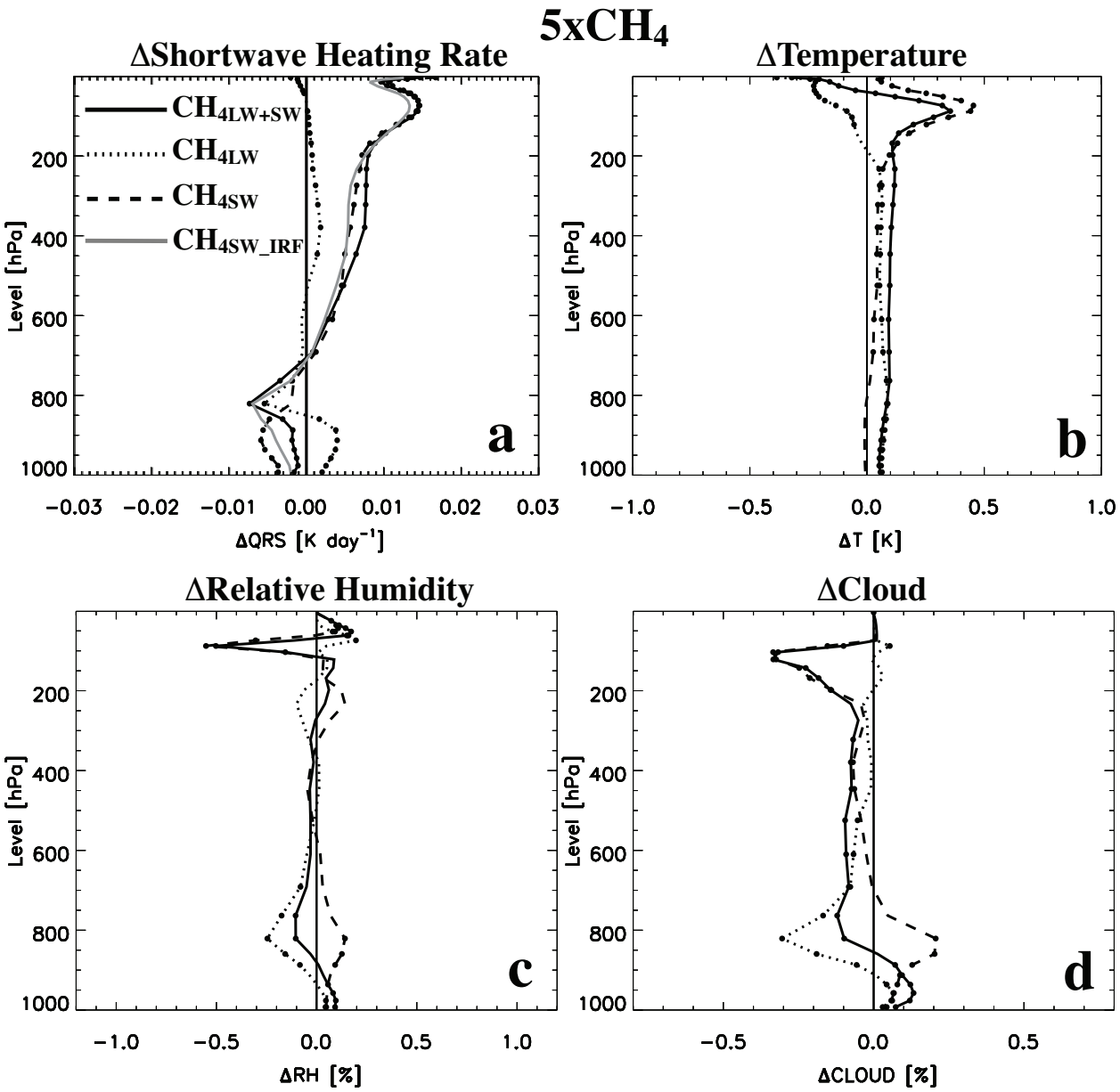

SUPPLEMENTARY FIGURE 3 **Global annual mean vertical profiles of fast responses for 5xCH$_4$.** Atmospheric (a) shortwave heating rate (QRS; [K day^{-1}]), (b) temperature (T; [K]), (c) relative humidity (RH; [%]) and (d) cloud fraction (CLOUD; [%]) for 5xCH$_4$. Panels include the contribution from 5xCH$_{4LW+SW}$ (solid black); 5xCH$_{4LW}$ (dotted), and 5xCH$_{4SW}$ (dashed). Solid dots represent a significant response at the 90% confidence level, based on a standard *t*-test. Fast responses are estimated from the fixed SST experiments. Also included in (a) is the instantaneous shortwave heating rate profile (5xCH$_{4SW\text{-}IRF}$; gray), as calculated by the offline radiative transfer model, PORT.

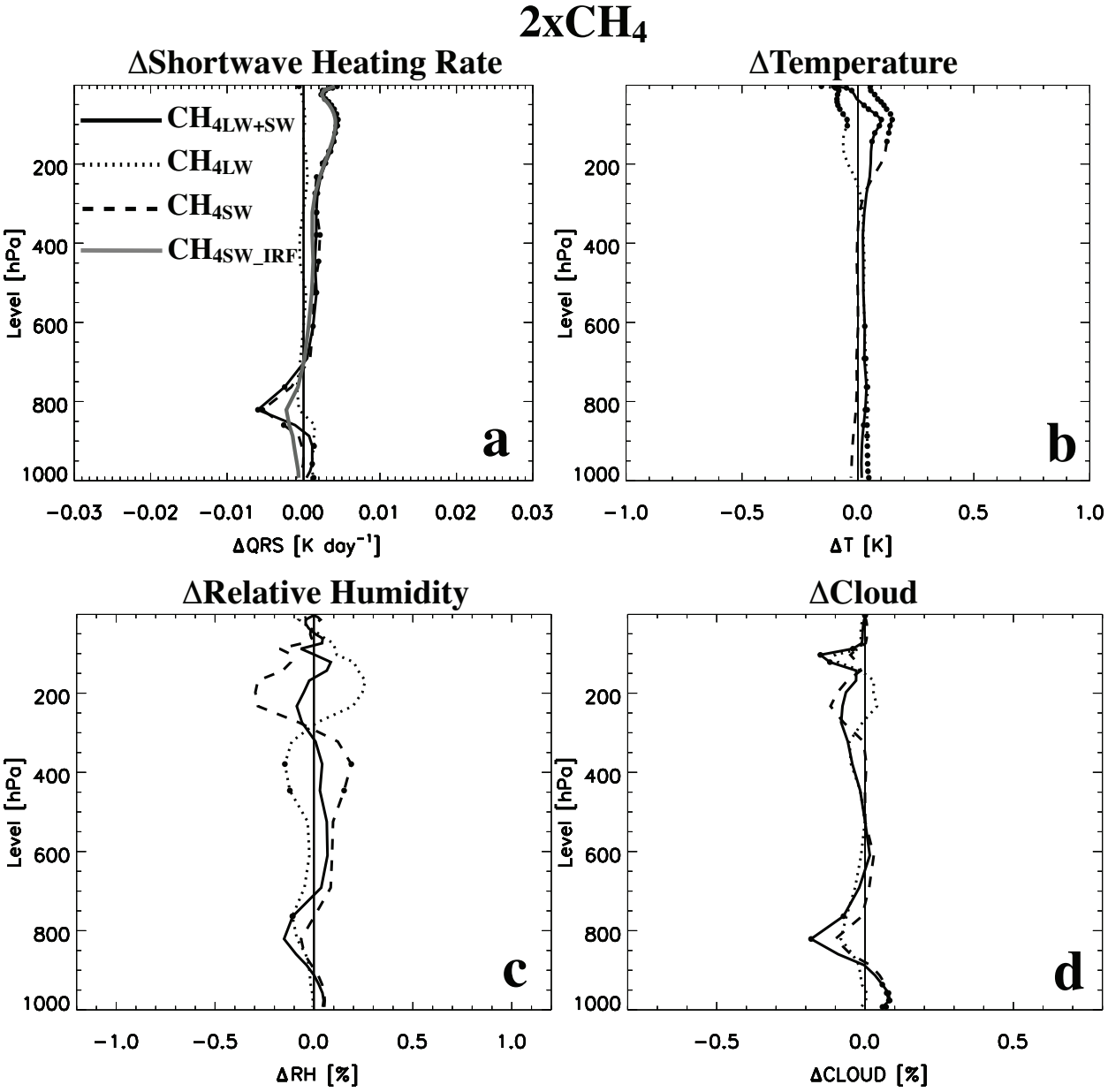

Supplementary Figure 4 **Global annual mean vertical profiles of fast responses for 2xCH_4.** Atmospheric (a) shortwave heating rate (QRS; [K day^{-1}]), (b) temperature (T; [K]), (c) relative humidity (RH; [%]) and (d) cloud fraction (CLOUD; [%]) for 2xCH_4. Panels include the contribution from 2xCH_{4LW+SW} (solid black); 2xCH_{4LW} (dotted), and 2xCH_{4SW} (dashed). Solid dots represent a significant response at the 90% confidence level, based on a standard t-test. Fast responses are estimated from the fixed SST experiments. Also included in (a) is the instantaneous shortwave heating rate profile (2x$CH_{4SW\text{-}IRF}$; gray), as calculated by the offline radiative transfer model, PORT.

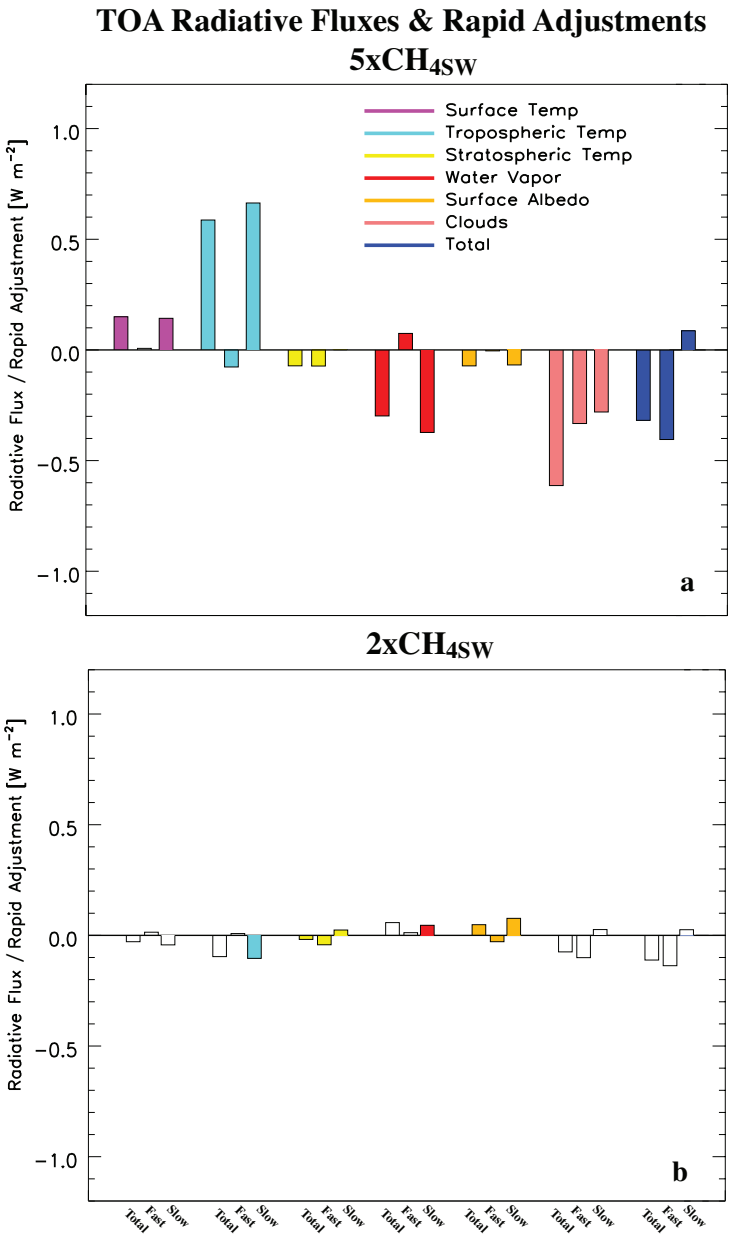

SUPPLEMENTARY FIGURE 5 **Top-of-the-atmosphere radiative flux decomposition for the total response, rapid adjustment and feedback under 5x and 2xCH_{4SW}.** Global annual mean top-of-the-atmosphere (TOA) surface temperature (purple), tropospheric temperature (cyan), stratospheric temperature (yellow), water vapor (red), surface albedo (orange), cloud (pink) and total (blue) radiative flux decomposition for (a) 5xCH_{4SW} and (b) 2xCH_{4SW}. The first bar in each like-colored set of three bars represents the total response (from the coupled ocean simulations); the second bar represents the rapid adjustment (i.e., fast response); and the third bar represents the surface-temperature induced feedback (i.e., slow response). Responses not significant, based on a standard t-test at the 90% confidence level, have unfilled bars. These uncertainties are therefore relative to interannual variability. Surface temperature induced (unnormalized) feedbacks are estimated by subtracting the rapid adjustments (from fixed SST experiments) from the corresponding radiative kernel decomposition applied to the coupled experiments. Units are W m^{-2}.

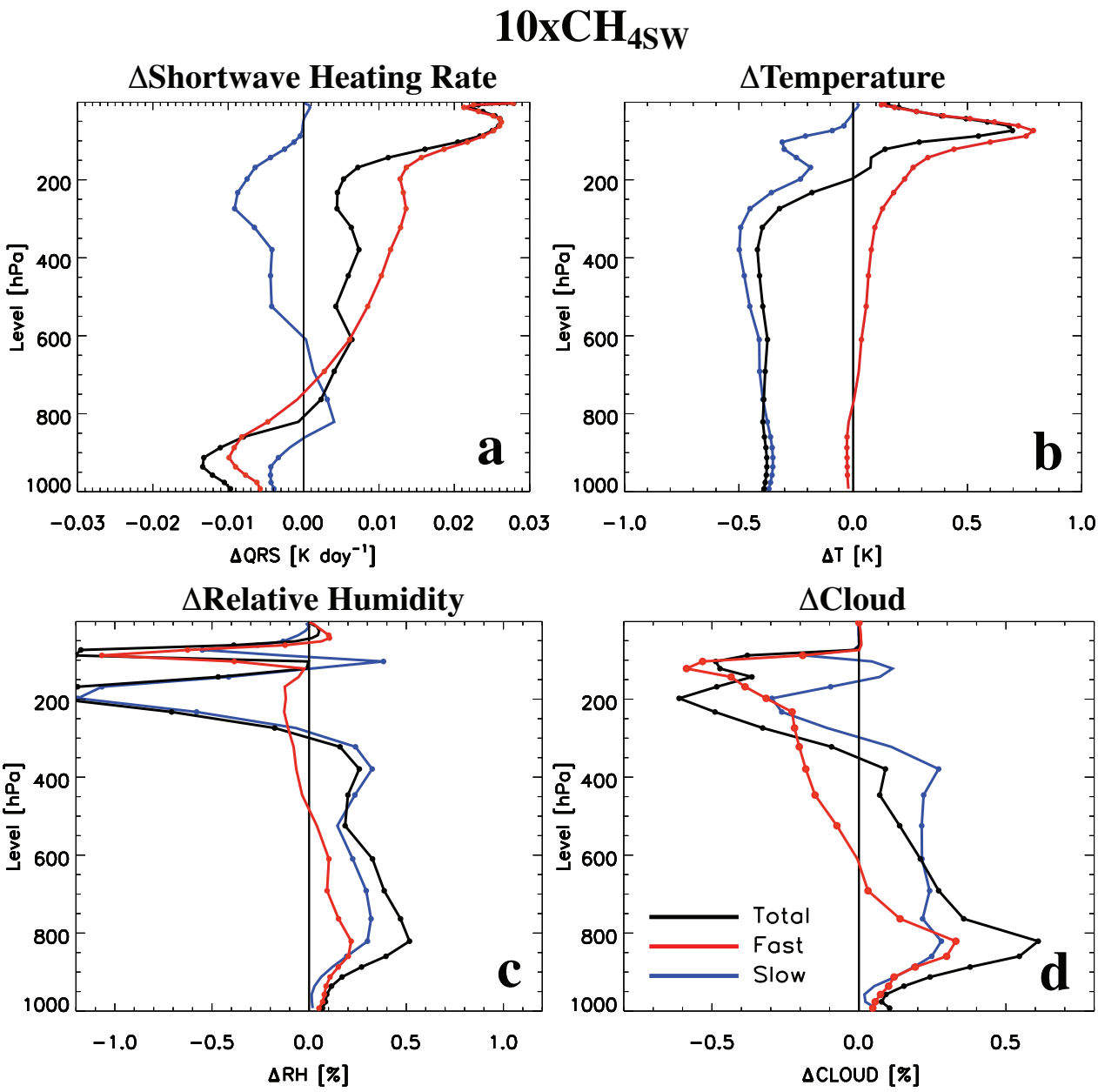

SUPPLEMENTARY FIGURE 6 **Global annual mean vertical profiles of the total response, rapid adjustment and feedback under 10xCH$_{4SW}$.** Atmospheric (a) shortwave heating rate (QRS; [K day^{-1}]), (b) temperature (T; [K]), (c) relative humidity (RH; [%]) and (d) cloud fraction (CLOUD; [%]) for 10xCH$_{4SW}$. Panels include the total response (black), rapid adjustment (i.e., fast response; red) and surface-temperature-induced feedback (i.e., slow response; blue). Solid dots represent a significant response at the 90% confidence level, based on a standard t-test. The total response comes from the coupled ocean experiment and the fast response comes from the fixed SST experiment. The slow response, which isolates the surface temperature induced (unnormalized) feedback, is estimated by subtracting the fast response from the total response.

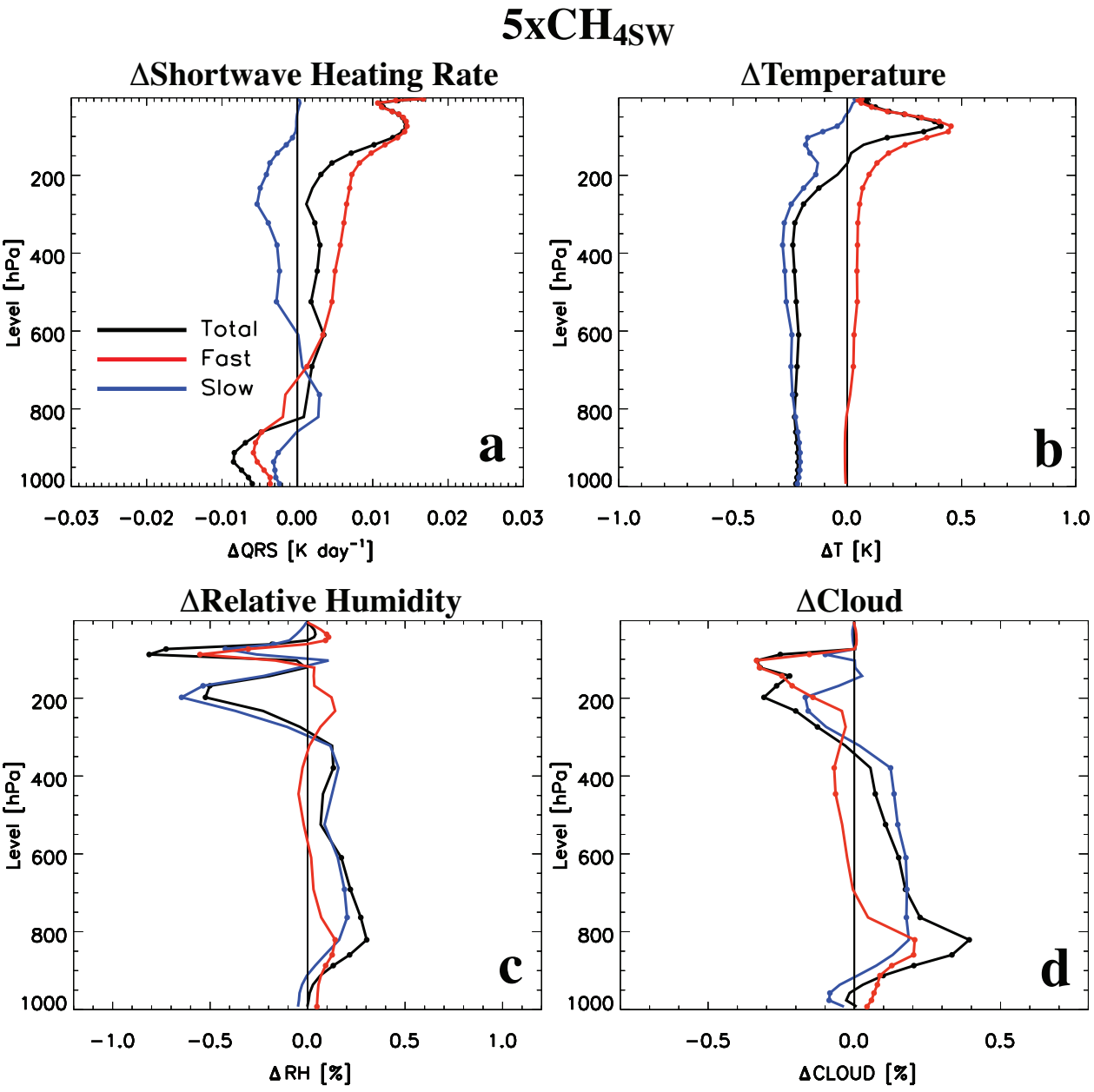

SUPPLEMENTARY FIGURE 7 **Global annual mean vertical profiles of the total response, rapid adjustment and feedback under 5xCH$_{4SW}$.** Atmospheric (a) shortwave heating rate (QRS; [K day^{-1}]), (b) temperature (T; [K]), (c) relative humidity (RH; [%]) and (d) cloud fraction (CLOUD; [%]) for 5xCH$_{4SW}$. Panels include the total response (black), rapid adjustment (i.e., fast response; red) and surface-temperature-induced feedback (i.e., slow response; blue). Solid dots represent a significant response at the 90% confidence level, based on a standard *t*-test. The total response comes from the coupled ocean experiment and the fast response comes from the fixed SST experiment. The slow response, which isolates the surface temperature induced (unnormalized) feedback, is estimated by subtracting the fast response from the total response.

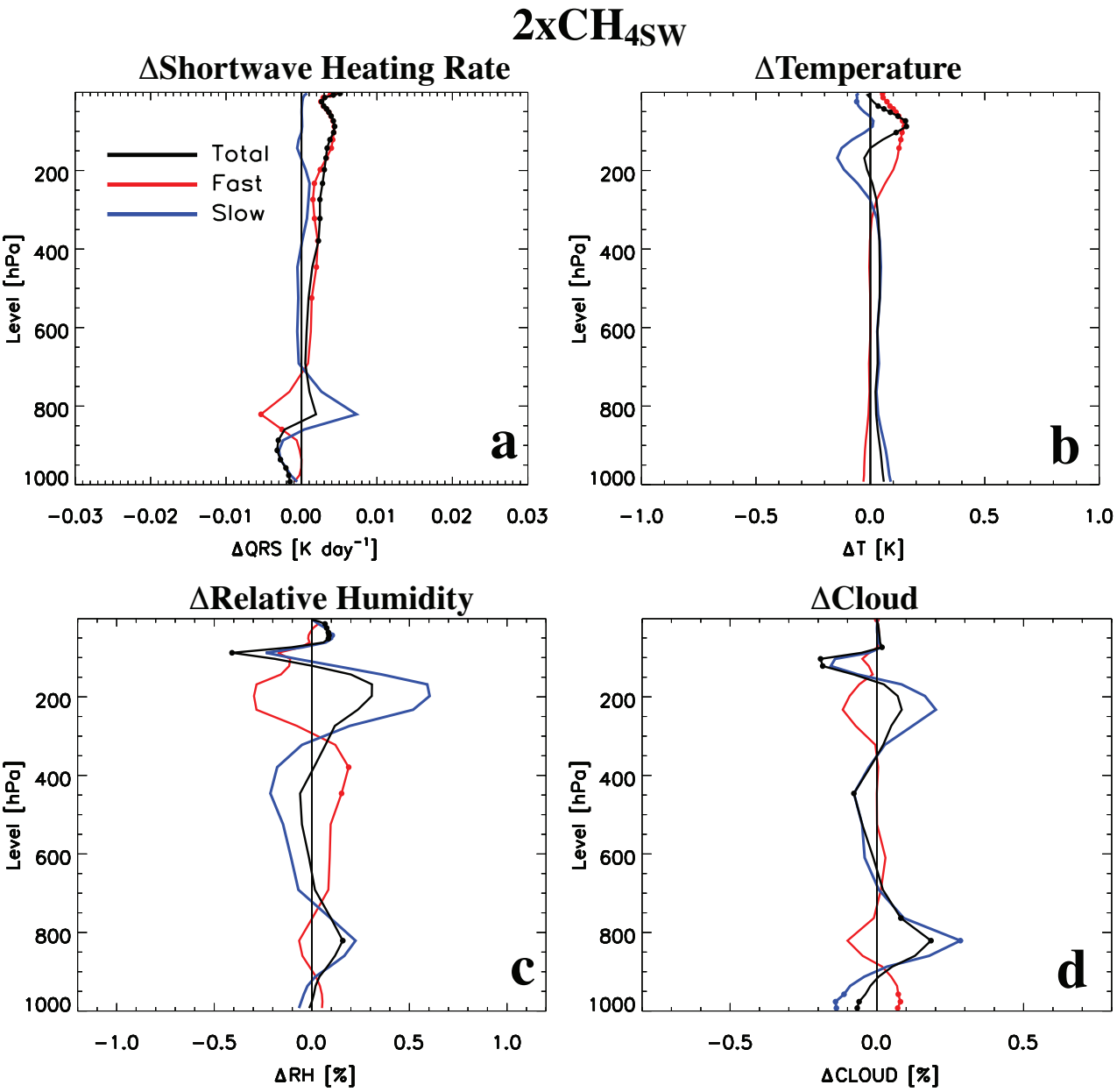

SUPPLEMENTARY FIGURE 8 **Global annual mean vertical profiles of the total response, rapid adjustment and feedback under 2xCH$_{4SW}$.** Atmospheric (a) shortwave heating rate (QRS; [K day^{-1}]), (b) temperature (T; [K]), (c) relative humidity (RH; [%]) and (d) cloud fraction (CLOUD; [%]) for 2xCH$_{4SW}$. Panels include the total response (black), rapid adjustment (i.e., fast response; red) and surface-temperature-induced feedback (i.e., slow response; blue). Solid dots represent a significant response at the 90% confidence level, based on a standard *t*-test. The total response comes from the coupled ocean experiment and the fast response comes from the fixed SST experiment. The slow response, which isolates the surface temperature induced (unnormalized) feedback, is estimated by subtracting the fast response from the total response.